Autophagy 11:6, 881–890; June 2015; © 2015 Taylor and Francis Group, LLC

The autophagy gene *Wdr45/Wipi4* regulates learning and memory function and axonal homeostasis

Yan G Zhao,[1] Le Sun,[2] Guangyan Miao,[1] Cuicui Ji,[1] Hongyu Zhao,[1] Huayu Sun,[1] Lin Miao,[3] Saori R. Yoshii,[4] Noboru Mizushima,[4] Xiaoqun Wang,[2] and Hong Zhang[1,*]

[1]State Key Laboratory of Biomacromolecules; Institute of Biophysics; Chinese Academy of Sciences; Beijing, China; [2]State Key Laboratory of Brain and Cognitive Science; Institute of Biophysics; Chinese Academy of Sciences; Beijing, China; [3]National Institute of Biological Sciences; Beijing, China; [4]Department of Biochemistry and Molecular Biology; Graduate School and Faculty of Medicine; University of Tokyo; Bunkyo-ku, Tokyo, Japan

Keywords: autophagy, axon swelling, learning and memory, neurodegeneration, *Wdr45/Wipi4*

Abbreviations: ACTB, β-actin; AMC, aminomethylcoumarin; *Atg*, autophagy-related; BPAN, β-propeller protein-associated neurodegeneration; CALB, calbindin; CNS, central nervous system; DCN, deep cerebellar nuclei; *Ei24*, etoposide-induced gene 24; *epg*, ectopic P granule; fEPSP, field excitatory postsynaptic potential; GFAP, glial fibrillary acid protein; H&E, hematoxylin and eosin; KO, knockout; LC3, microtubule-associated protein 1 light chain 3; LTP, long-term potentiation; MBP, myelin basic protein; NBIA, neurodegeneration with brain iron accumulation; RBFOX3, RNA binding protein, fox-1 homolog (*C. elegans*) 3; rpm, rotations per min; SENDA, static encephalopathy of childhood with neurodegeneration in adulthood; SQSTM1, sequestosome-1; *WDR5/WIPI4*, WD repeat domain 45; WT, wild type.

WDR45/WIPI4, encoding a WD40 repeat-containing PtdIns(3)P binding protein, is essential for the basal autophagy pathway. Mutations in *WDR45* cause the neurodegenerative disease β-propeller protein-associated neurodegeneration (BPAN), a subtype of NBIA. We generated CNS-specific *Wdr45* knockout mice, which exhibit poor motor coordination, greatly impaired learning and memory, and extensive axon swelling with numerous axon spheroids. Autophagic flux is defective and SQSTM1 (sequestosome-1)/p62 and ubiquitin-positive protein aggregates accumulate in neurons and swollen axons. *Nes-Wdr45*$^{fl/Y}$ mice recapitulate some hallmarks of BPAN, including cognitive impairment and defective axonal homeostasis, providing a model for revealing the disease pathogenesis of BPAN and also for investigating the possible role of autophagy in axon maintenance.

Introduction

Autophagy is a lysosome-mediated degradation system, in which a portion of cytosol is engulfed in an enclosed double-membrane vesicle, termed the autophagosome, and subsequently delivered to the lysosome for degradation.[1] A group of evolutionarily conserved *Atg* (autophagy-related) genes and metazoan-specific *epg* (ectopic P granule) genes, including *epg-3, -4, -5*, and *-6*, has been identified from yeast and worm genetic studies that act at distinct steps of the autophagy pathway in higher eukaryotes.[1-3] The basal constitutive level of autophagy functions as a quality control mechanism by removing misfolded proteins and/or damaged organelles.[4] Under physiological conditions, autophagy is crucial for maintaining neuron homeostasis. Mice deficient in autophagy genes essential for autophagosome formation, such as *Atg5, Atg7*, and *Ei24* (etoposide-induced gene 24, the mammalian ortholog of *Caenorhabditis elegans epg-4*), exhibit massive neuron loss and axonal degeneration, accompanied by dramatic accumulation of ubiquitinated protein aggregates.[5-7]

Recent human genetic studies reveal that de novo mutations in *WDR45* (WD repeat domain 45) cause BPAN, previously known as SENDA (static encephalopathy of childhood with neurodegeneration in adulthood), which is a subtype of neurodegeneration with brain iron accumulation (NBIA).[8-10] Mammalian *WDR45* is the ortholog of worm *epg-6* and one of the orthologs of yeast *Atg18* and is essential for an early step of autophagosome formation.[3] NBIA encompasses a heterogeneous group of progressive extrapyramidal disorders characterized by parkinsonism, intellectual deterioration, deposition of iron in the basal ganglia, and pathologically, the presence of axonal spheroids in the CNS (central nervous system).[11,12] BPAN patients have static encephalopathy in childhood, characterized by psychomotor retardation with or without concurrent spasticity, and then develop sudden-onset dystonia-parkinsonism and dementia in adulthood.[12] Samples from affected BPAN patients display lower autophagic activity and accumulation of aberrant early autophagic structures, suggesting that *WDR45* functions in maintaining neural homeostasis through its role in autophagy.[10]

*Correspondence to: Hong Zhang; Email: hongzhang@sun5.ibp.ac.cn
Submitted: 10/31/2014; Revised: 04/16/2015; Accepted: 04/27/2015
http://dx.doi.org/10.1080/15548627.2015.1047127

To study the relationship between *WDR45* and neurodegeneration, we generated CNS-specific *Wdr45* knockout (KO) mice. These mice displayed learning and memory defect and axonal swelling. *Wdr45* deficiency impaired the autophagic flux with accumulation of SQSTM1- and ubiquitin-positive aggregates in neurons and swollen axons. Our study indicates that the *Nes-Wdr45*$^{fl/Y}$ mice exhibit hallmarks of BPAN, providing a model for understanding the neurodegeneration process underlying the pathogenesis of BPAN.

Results

Nes-Wdr45$^{fl/Y}$ mice develop learning and memory impairments

We generated conditional KO mice by flanking exons 8 to 14 of *Wdr45* with 2 *Loxp* sequences (**Fig. 1A and B**). *Wdr45* locates on the X chromosome. *Wdr45*$^{fl/fl}$ mice were crossed with *Nes-Cre* mice to produce CNS-specific *Wdr45* knockout mice. Real-time PCR confirmed the absence of *Wdr45* mRNA in various parts of the CNS in *Nes-Wdr45*$^{fl/Y}$ mice (**Fig. 1C**). *Nes-Wdr45*$^{fl/Y}$ mice were born normally, and showed no obvious growth retardation. Neither motor dysfunctions, such as tremor, hypokinesia, rigidity and dystonia, nor limb-clasping reflexes were evident in *Nes-Wdr45*$^{fl/Y}$ mice. Rotarod experiments were performed to examine motor coordination. *Nes-Wdr45*$^{fl/Y}$ mice at 7 to 8 mo showed no significant difference at 20 rotations per min (rpm) (**Fig. 1D**), but *Nes-Wdr45*$^{fl/Y}$ mice at 11 to 13 mo spent less time on the rotarod compared to their wild-type (WT) littermates when assessed at higher than 5 rpm (**Fig. 1E**), indicating that aged *Nes-Wdr45*$^{fl/Y}$ mice showed impaired motor coordination.

The hallmark neurological defect associated with BPAN is intellectual deterioration.[12] We thus performed a series of behavioral tests to determine the learning and memory ability of *Nes-Wdr45*$^{fl/Y}$ mice. Since the performances of female animals change during various phases of the estrous cycle,[13] we analyzed only males. The Morris water maze test involves recognizing and remembering visual cues to locate a hidden platform, thus measuring learning and memory function. In training sessions, *Nes-Wdr45*$^{fl/Y}$ mice showed significantly prolonged latency to find the hidden platform compared to controls (**Fig. 1F**). Furthermore, *Nes-Wdr45*$^{fl/Y}$ mice spent significantly less time in the target quadrant than control littermates without the platform during the probe sessions, suggesting impaired retention of spatial memory (**Fig. 1G**). Swimming speeds were similar for *Nes-Wdr45*$^{fl/Y}$ and control mice (**Fig. 1H**). In a Y-maze test for spontaneous alternation behavior, *Nes-Wdr45*$^{fl/Y}$ mice were less likely than controls to explore alternate arms of the Y-maze within an 8-min test period, reflecting impaired immediate spatial working memory performance (**Fig. 1I**). In a fear conditioning test, on the training day, mice were placed in a chamber and received paired conditioned stimulus (a 70 dB tone) and adverse stimulus (an electric foot shock). On the testing day, in the contextual test, *Nes-Wdr45*$^{fl/Y}$ mice showed a significant decrease in freezing time compared to controls when the mice were put in the same chamber, indicating that *Wdr45* deficiency causes impaired fear recall in the same context. In the cued test, *Nes-Wdr45*$^{fl/Y}$ mice displayed no significant difference in the freezing response with the conditioned stimulus, compared with WT mice (**Fig. 1J**). Thus, *Nes-Wdr45*$^{fl/Y}$ mice show significant deficits in cognitive function.

The hippocampus plays a crucial role in the consolidation of information from short-term memory to long-term memory and spatial navigation.[14] Long-term potentiation (LTP), a well-characterized form of synaptic plasticity, has been postulated as a cellular correlate of learning and memory.[15] To investigate whether the behavioral deficits in *Nes-Wdr45*$^{fl/Y}$ mice were associated with altered hippocampal synaptic plasticity, LTP was evaluated at Schaffer Collateral (SC)-CA1 synapses in hippocampal slices induced by θ-burst stimulation. LTP was significantly attenuated in *Nes-Wdr45*$^{fl/Y}$ mice, as indicated by the decreased field excitatory postsynaptic potential (fEPSP) amplitude (**Fig. 1K and L**). This is consistent with the defect in learning and memory in *Nes-Wdr45*$^{fl/Y}$ mice.

Axonal swelling in *Nes-Wdr45*$^{fl/Y}$ mice

To investigate the neural defect in *Nes-Wdr45*$^{fl/Y}$ mice, we performed histological analyses on sections from CNS of control and *Nes-Wdr45*$^{fl/Y}$ mice at 13 mo. No extensive or selective neuron loss was observed, unlike in mice deficient in several other autophagy genes.[5-7,16] The number of Purkinje cells in the cerebellum and hippocampus pyramidal cells in the CA1 region showed no significant change in *Nes-Wdr45*$^{fl/Y}$ mice compared to controls (**Fig. 2A and B**). GFAP (glial fibrillary acid protein) staining showed mild reactive astrogliosis in various brain regions of *Nes-Wdr45*$^{fl/Y}$ mice, including the cortex, hippocampus, thalamus, hypothalamus, caudate nucleus, deep cerebellar nuclei (DCN), and pons (**Fig. 2C–E**, and data not shown). Thus, *Wdr45* deficiency causes mild neural damage.

White matter changes are pathological features associated with BPAN.[12] We next determined whether homeostasis of myelinated axons is affected by *Wdr45* deficiency. Hematoxylin and eosin (H&E) staining revealed that eosinophilic spheroids, representing axon swellings, were scattered in various cerebral regions, including cortex, thalamus, and hypothalamus (**Fig. 2F**, and data not shown). Clusters of vacuolated structures were found in the thalamus, inferior colliculus, and medulla of *Nes-Wdr45*$^{fl/Y}$ mice (**Fig. 2G** and data not shown). We also examined the cerebellar white matter. Numerous large eosinophilic spheroid structures were observed in the DCN, indicative of axonal swellings (**Fig. 2H and I**). We further stained the DCN region with anti-CALB/calbindin antibody, which specifically labels Purkinje cell axons, and found that a large number of huge bulging CALB-positive structures (some of them surrounded by MBP (myelin basic protein)-labeled myelin) were present in *Nes-Wdr45*$^{fl/Y}$ mice, indicating Purkinje cell axonal swellings (**Fig. 2J and K**). Ultrastructural study further confirmed accumulation of swollen axons in the DCN of *Nes-Wdr45*$^{fl/Y}$ mice (**Fig. 2L and M**), and abundant swollen mitochondria were found in these axons (**Fig. 2N and O**). Demyelinated axons were also detected, as shown in **Figure 2P**. We occasionally found degenerated axons in the DCN (**Fig. 2Q**) and medulla of *Nes-Wdr45*$^{fl/Y}$ mice

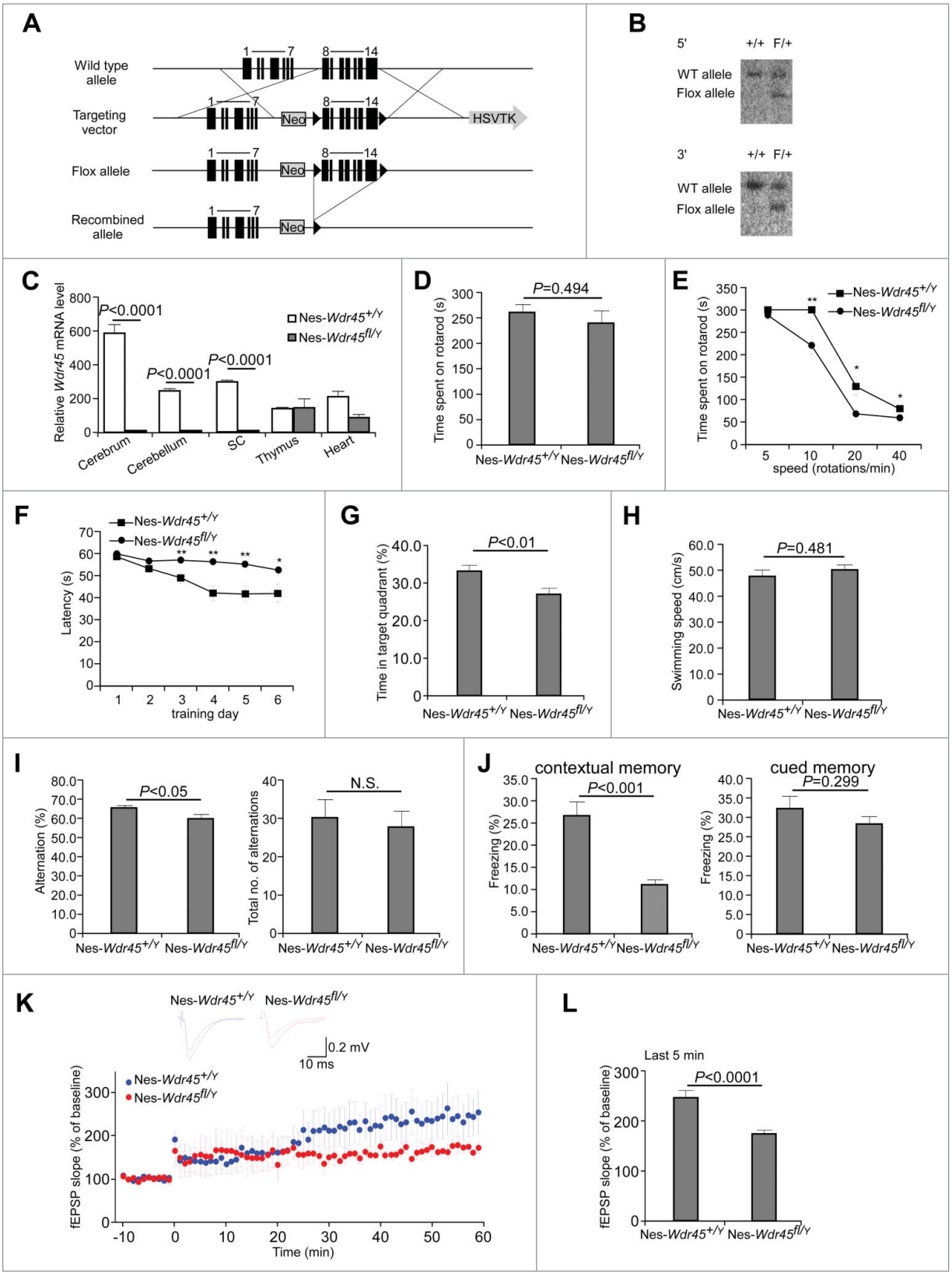

Figure 1. For figure legend, see page 884.

(**Fig. 2R and S**). We analyzed brain sections at 6 wk and 4 mo and found that eosinophilic spheroids were formed progressively (**Fig. 2T–X**). Thus, *Wdr45* plays a critical function in axon homeostasis.

Accumulation of SQSTM1- and ubiquitin-positive aggregates in *Nes-Wdr45*$^{fl/Y}$ mice

To assess whether the autophagic flux is impaired in *Nes-Wdr45*$^{fl/Y}$ mice, we performed immunostaining of brain sections to detect SQSTM1 and ubiquitin, 2 well-characterized autophagy substrates that are elevated after inhibition of autophagy.[17] Compared to *Nes-Wdr45*$^{+/Y}$ mice, in some brain regions of *Nes-Wdr45*$^{fl/Y}$ mice, including thalamus, DCN, and medulla, both SQSTM1- and ubiquitin-positive aggregates accumulated, and these aggregates largely colocalized with each other (**Fig. 3A and B** and data not shown). Accumulation of ubiquitin-positive aggregates was also found in the caudate nucleus and the molecular layer of the dentate gyrus of the hippocampus in *Nes-Wdr45*$^{fl/Y}$ mice, without evident SQSTM1 accumulation (**Fig. 3C and D**). *Sqstm1* mRNA levels were not upregulated in *Nes-Wdr45*$^{fl/Y}$ mice (**Fig. 3E**). Proteasome activity was not altered in brain extracts of *Nes-Wdr45*$^{fl/Y}$ mice (**Fig. 3F**). Our previous study shows that loss of function of *epg-6* causes accumulation of ATG-9 puncta.[3] Immunostaining assays demonstrated that ATG9-positive structures were also moderately increased in the DCN region of *Nes-Wdr45*$^{fl/Y}$ mice (**Fig. 3G and H**).

We costained SQSTM1 with different neural cell markers to determine which type of neural cell is affected by *Wdr45* deficiency. In *Nes-Wdr45*$^{fl/Y}$ mice, neurons detected by anti-RBFOX3/NeuN (RNA binding protein, fox-1 homolog [*C. elegans*] 3), including pyramidal cells in hippocampus and cortex, contained SQSTM1 aggregates (**Fig. 3I and J**), while SQSTM1 accumulation was hardly observed in oligodendrocytes (data not shown). In the DCN region, ubiquitin and CALB costaining assays revealed that ubiquitin-positive aggregates were present in small axon spheroids but were mostly absent from large ones (**Fig. 3K**), suggesting that the ubiquitin inclusions became diffuse or were removed during later axon swelling.

To directly detect whether *Wdr45* deficiency blocks neuronal autophagic flux, we cultured primary neurons from WT and *Nes-Wdr45*$^{fl/Y}$ mice. Immunoblotting assays revealed that levels of LC3 (Microtubule-associated protein 1 light chain 3)-I, LC3-II, and SQSTM1 increased in *Wdr45* KO neurons (**Fig. 3L and M**). After treatment with bafilomycin A_1, a potent inhibitor of the vacuolar H^+ ATPase that inhibits the lysosomal degradation of LC3-II, there is no difference of LC3-II level between control and mutant cells (**Fig. 3N and O**), suggesting that autophagic flux is impaired in *Wdr45*-deficient neurons.

Axonal swelling and autophagy defects in female *Nes-Wdr45*$^{fl/fl}$ mice

As *Wdr45* locates on the X chromosome, we examined whether there is a gender-dependent difference in the axonal swelling and autophagy defects. Numerous eosinophilic spheroids accumulated in female *Nes-Wdr45*$^{fl/fl}$ mice, just as in males (**Fig. 4A**). Real-time PCR confirmed the absence of *Wdr45* mRNA in the cerebrum of *Nes-Wdr45*$^{fl/fl}$ mice (**Fig. 4B**). The *Wdr45* mRNA level in the cerebrum of *Nes-Wdr45*$^{fl/+}$ mice was also reduced compared to WT mice (**Fig. 4B**). Dilated axons, detected by anti-CALB and anti-MBP costaining, were present, and SQSTM1- and ubiquitin-positive aggregates accumulated in the DCN of female *Nes-Wdr45*$^{fl/+}$ mice and *Nes-Wdr45*$^{fl/fl}$ mice. The defects in the heterozygous mice are less severe than in the homozygous mice (**Fig. 4C–F**).Therefore, similar to male *Wdr45*mutant mice, female *Wdr45*-deficient mice also displayed axon swelling and autophagy defects.

Discussion

Here we show that CNS-specific *Wdr45* KO mice develop axonal swelling and behavioral abnormalities, including motor deficits and learning and memory impairment. The cognitive defects in *Nes-Wdr45*$^{fl/Y}$ mice may be associated with impaired axon homeostasis and/or accumulation of ubiquitin-positive inclusions in the hippocampus and caudate nucleus. Previous study has reported that lesions of the hippocampus affect fear conditioning to the context but not to the cue, while damage of the amygdala interferes with the conditioning to both the cue and the context.[18] *Nes-Wdr45*$^{fl/Y}$ mice display obvious

Figure 1. (See previous page) *Nes-Wdr45*$^{fl/Y}$ mice show cognitive impairment and LTP attenuation. (**A**) Scheme for generating *Wdr45* conditional knockout mice. (**B**) Southern blot analysis of genomic DNA from +/+ and F/+ ES clones. After digestion with SpeI, the WT and flox alleles were detected as 12- and 7.7-kb bands with a 5′ probe, respectively. After digestion with NdeI, the WT and flox alleles were detected as 14- and 8.4-kb bands with 3′ probe, respectively. (**C**) *Wdr45* mRNA level in different tissues of WT and *Nes-Wdr45*$^{fl/Y}$ mice at 13 mo. Results are representative of at least 3 experiments. Compared to WT mice, the *Wdr45* mRNA level is slightly decreased in the heart of *Nes-Wdr45*$^{fl/Y}$mice, probably due to nonspecific expression of *Nes-Cre* (http://cre.jax.org/Nes/Nes-CreNano.html). (**D**) Rotarod performance of *Nes-Wdr45*$^{fl/Y}$ and *Nes*-Wdr45$^{fl/+}$ mice (7 to 8 mo) at rolling speed of 20 rpm. Mean ±SEM of 11 mice is shown. (**E**) Rotarod performance of *Nes-Wdr45*$^{fl/Y}$ and *Nes-Wdr45*$^{fl/+}$ mice at rolling speeds of 5, 10, 20, and 40 rpm. *, $P < 0.05$; **, $P < 0.01$. (**F–H**) In the Morris water maze test, *Nes-Wdr45*$^{fl/Y}$mice show decreased learning and memory ability in the learning and probe test, respectively. The swimming speeds show no obvious difference between *Nes-Wdr45*$^{+/Y}$ and *Nes-Wdr45*$^{fl/Y}$ mice. (**I**) *Nes-Wdr45*$^{fl/Y}$ mice display a reduced percentage of correct alternations, compared with *Nes-Wdr45*$^{+/Y}$ mice in a Y-maze test. No obvious difference in the total number of alternations was detected between WT and *Nes-Wdr45*$^{fl/Y}$ mice. (**J**) In a contextual fear conditioning test, the percentage of the test time taken up by a freezing response is significantly lower in *Nes-Wdr45*$^{fl/Y}$ mice. In a cued test, the freezing time is slightly reduced in *Nes-Wdr45*$^{fl/Y}$mice. Mean ±SEM of 11 mice (11 to 13 mo) is shown (**C–H**). (**K and L**) Impaired LTP in *Nes-Wdr45*$^{fl/Y}$ mice. The upper part in (**K**) shows averaged fEPSPs comparing baseline and the last 5 min in *Nes-Wdr45*$^{+/Y}$ and *Nes-Wdr45*$^{fl/Y}$ mice. LTP was not induced in 7 out of 11 hippocampal slices from 3 *Nes-Wdr45*$^{fl/Y}$ mice, while LTP was normally induced in all of 5 slices from 2 WT mice. Only slices with LTP induction were analyzed here. Averaged responses from the last 5 min in control and *Nes-Wdr45*$^{fl/Y}$ mice (**L**).

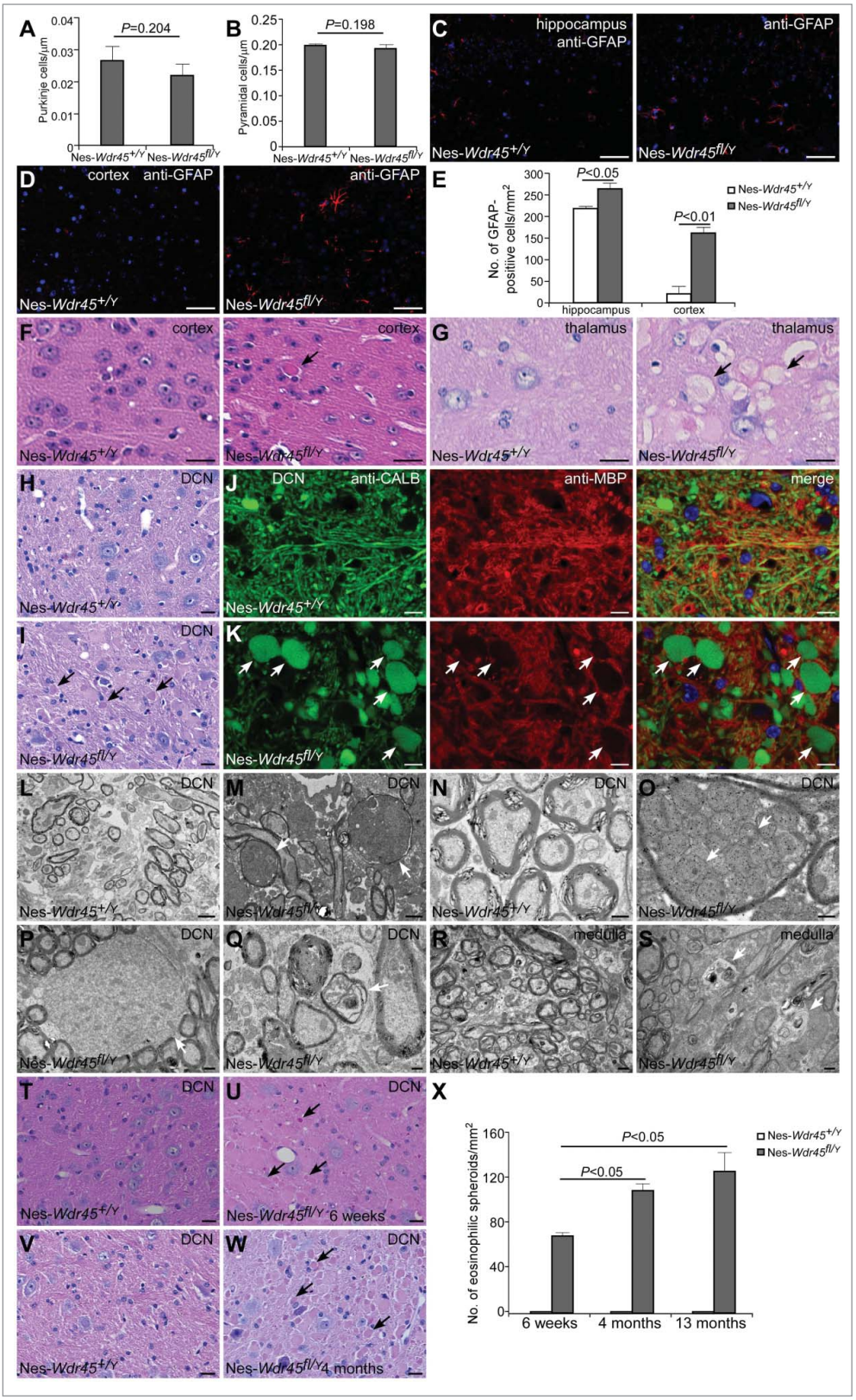

Figure 2. *Nes-Wdr45*$^{fl/Y}$ mice show axon swelling. (**A**) The number of Purkinje cells was quantified and divided by the total length of the lobules III, IV and V. (**B**) The number of CA1 hippocampal pyramidal cells of *Nes-Wdr45*$^{+/Y}$ and *Nes-Wdr45*$^{fl/Y}$ mice at 13 mo was quantified and divided by the length of the layer. Mean ± SEM of 3 mice is shown (**A and B**). (**C–E**) Compared to control mice, the GFAP signals (red) in sections of hippocampus (**C**) and cortex (**D**) are stronger in *Nes-Wdr45*$^{fl/Y}$ mice. Quantification data are shown as mean ±SEM of 3 mice (**E**). Bar: 50μm. (**F**) H&E staining reveals the presence of eosinophilic spheroids (arrow) in the cortex. (**G**) H&E staining shows vacuolated structures (arrows) in thalamus. (**H and I**) H&E staining reveals the presence of eosinophilic spheroids (arrows) in the DCN of *Nes-Wdr45*$^{fl/Y}$ mice at 13 mo. Bar: 20 μm (**F–I**). (**J and K**) Costaining of CALB (green) and MBP (red) shows that *Nes-Wdr45*$^{fl/Y}$ mice at 13 mo exhibit dilated CALB-positive bulbs (arrows) in the DCN region. Bar: 10 μm. (**L to Q**) EM pictures of DCN in *Nes-Wdr45*$^{+/Y}$ (**L and N**) and *Nes-Wdr45*$^{fl/Y}$ (**M, O, P and Q**) mice at 13 mo. Arrows in (**M**) indicate swollen axons. Swollen mitochondria accumulate in these axons (arrows in **O**).The arrow in (**P**) indicates a demyelinated axon. Degenerated axons were also occasionally detected (**Q**). Bar: 2 μm (**L and M**), 500 nm (**N–Q**). (**R and S**) EM pictures of medulla in *Nes-Wdr45*$^{+/Y}$ (**R**) and *Nes-Wdr45*$^{fl/Y}$ (**S**) mice at 13 mo. Arrows in (**S**) indicate degenerated axons. Bar: 500 nm. (**T–X**) H&E staining of the DCN from *Wdr45* mutant mice and controls at 6 wk and 4 mo. Arrows indicate eosinophilic spheroids. Quantification data are shown as mean ±SEM of 3 mice (**X**). Bar: 20μm.

impairment in the contextual fear conditioning test, but not in the cued test, supporting that *Wdr45* deficiency mainly influences the function of hippocampus. This result is also in consistent with the attenuated LTP at SC-CA1 synapses in the hippocampus of *Nes-Wdr45*$^{fl/Y}$ mice. The poor motor coordination in *Nes-Wdr45*$^{fl/Y}$ mice is probably caused by the lesion in the DCN region of the cerebellum, which contributes to coordination, precision, and accurate timing of movements. *Nes-Wdr45*$^{fl/Y}$ mice show no signs of iron deposition in the basal ganglia. In NBIA, iron accumulation is variable and sometimes occurs later in the course of the disease after symptoms have

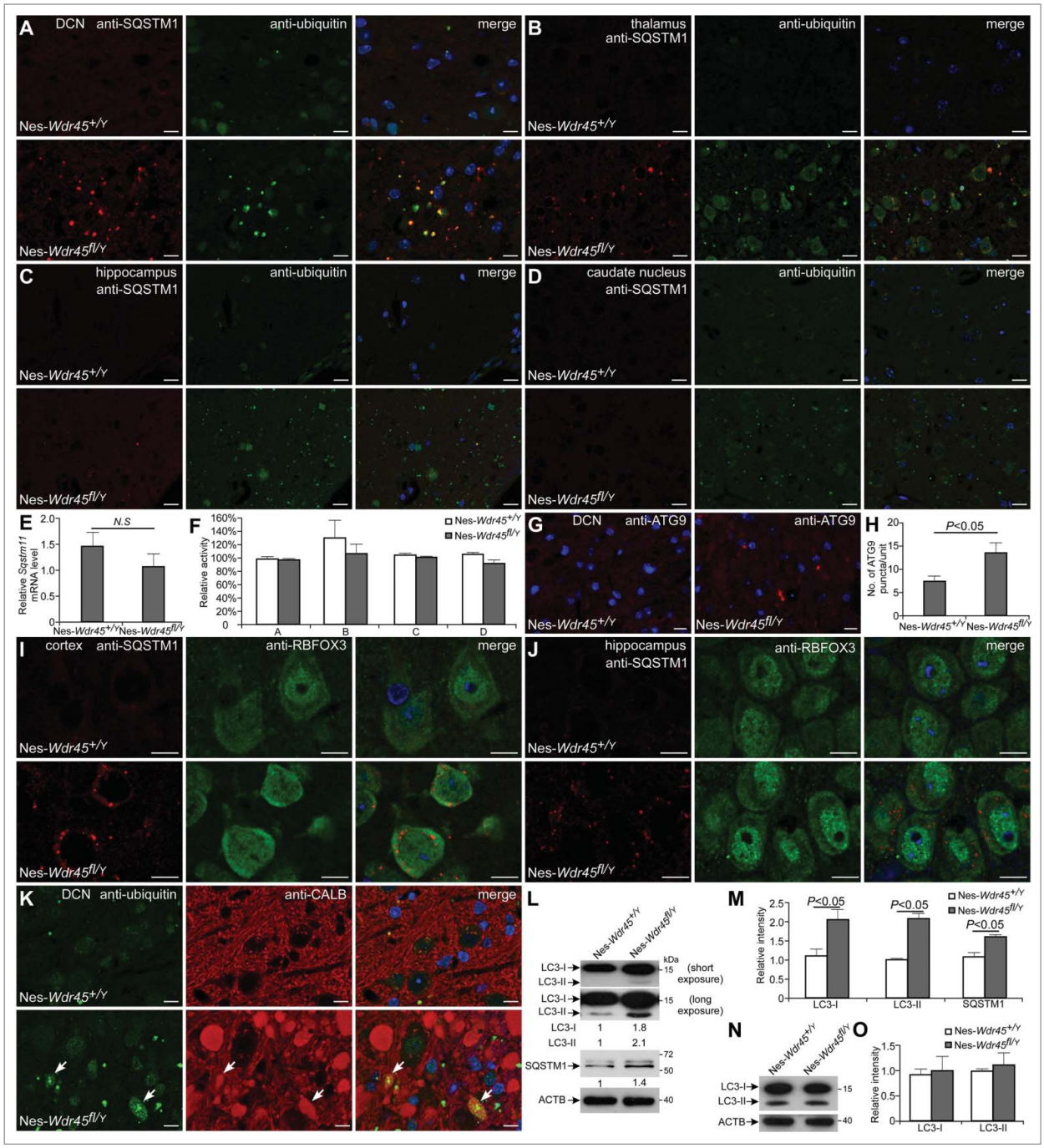

Figure 3. *Nes-Wdr45*$^{fl/Y}$ mice exhibit defective autophagic flux. (**A–D**) Coimmunostaining with anti-SQSTM1 (red) and anti-ubiquitin (green) antibodies in DCN (**A**), thalamus (**B**), hippocampus (**C**) and caudate nucleus (**D**) of *Nes-Wdr45*$^{fl/Y}$ mice at 13 mo. (**E**) No increase in the *Sqstm1* mRNA level is detected in *Nes-Wdr45*$^{fl/Y}$ mice. (**F**) Compared to control littermates, proteasome activity is not altered in brain extracts of *Nes-Wdr45*$^{fl/Y}$ mice at 13 mo. Proteasome activity was measured using AMC-linked substrate peptides. A: Ac-Gly-Pro-Leu-Asp-AMC; B: Suc-Leu-Leu-Val-Tyr-AMC; C: Ac-Arg-Leu-Arg-AMC; D: Boc-Leu-Arg-Arg-AMC. Results are representative of 2 experiments. (**G and H**) Anti-ATG9 staining shows that ATG9 puncta accumulate in the DCN of *Nes-Wdr45*$^{fl/Y}$ mice at 13 months. Quantification data are shown as mean ±SEM of 3 mice (1 unit = 10^4 μm^2) (**H**). (**I and J**) Anti-RBFOX3 (green) and anti-SQSTM1 (red) costaining shows that SQSTM1 aggregates are located in pyramidal neurons in the cortex (**I**) and hippocampus (**J**) of *Nes-Wdr45*$^{fl/Y}$ mice at 13 mo. (**K**) Anti-ubiquitin (green) and anti-CALB (red) costaining in the DCN of *Nes-Wdr45*$^{fl/Y}$ mice at 13 mo (arrows indicate dilated axonal terminals). Bar: 10 μm (**A–D, G, and I–K**). (**L and M**) Immunoblotting assays show that levels of LC3-I, LC3-II and SQSTM1 are increased in *Wdr45*-deficient neurons. Data are relative to ACTB level and representative of 3 independent experiments. (**N and O**) Immunoblotting assays show that levels of LC3-I and LC3-II are comparable between WT and *Wdr45*-deficient neurons after 6 h treatment with 20 μM bafilomycin A_1. Data are relative to ACTB level and representative of 3 independent experiments.

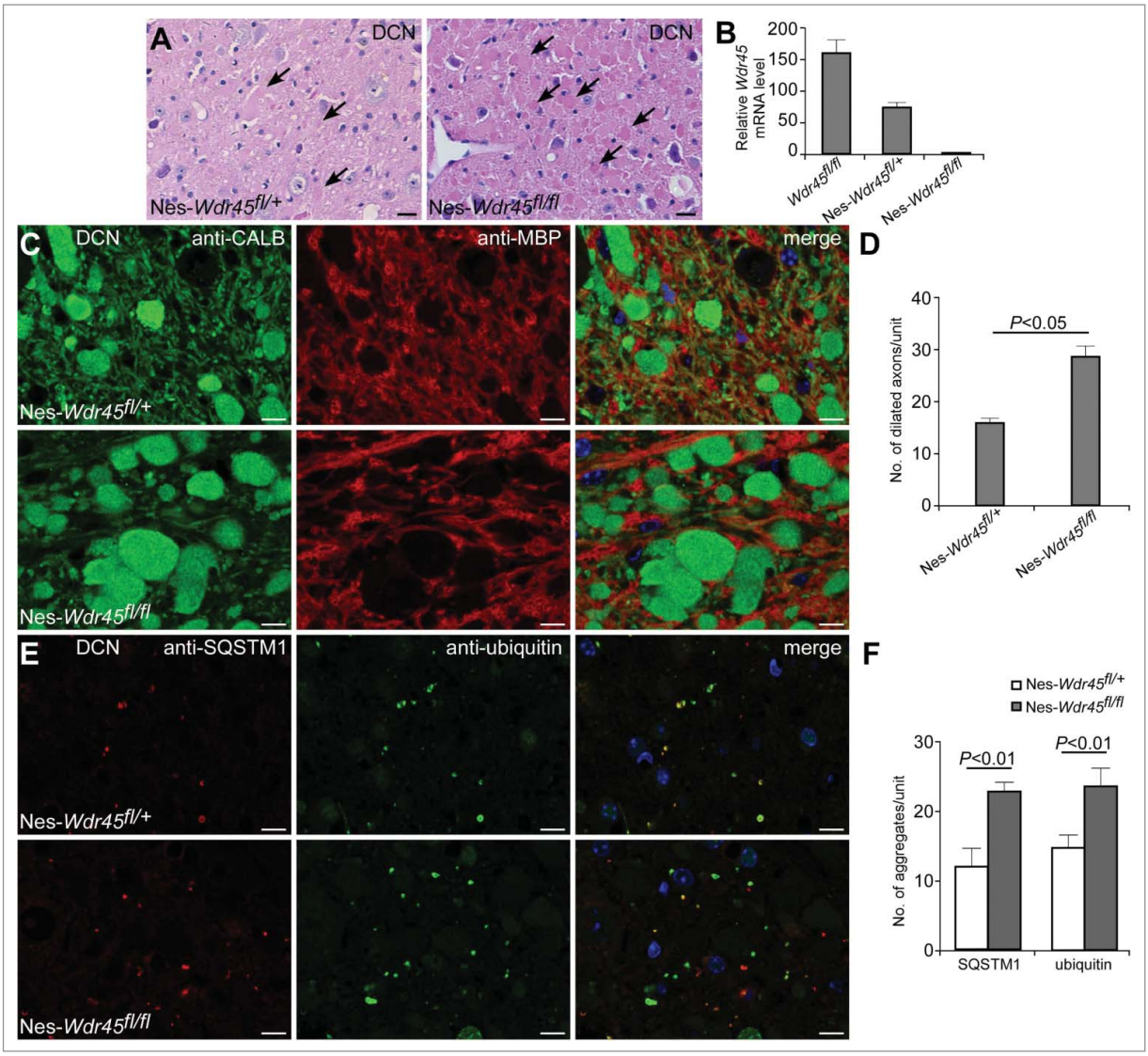

Figure 4. Axon swelling and autophagy defects in *Nes-Wdr45*$^{fl/fl}$ and *Nes-Wdr45*$^{fl/+}$ female mice. (**A**) H&E staining of cerebellar sections shows accumulation of eosinophilic spheroids (arrows) in both *Nes-Wdr45*$^{fl/+}$ and *Nes-Wdr45*$^{fl/fl}$ female mice at 13 mo. Bar: 20 μm. (**B**) The *Wdr45* mRNA level in the brain of WT, *Nes-Wdr45*$^{fl/+}$ mice and *Nes-Wdr45*$^{fl/fl}$ mice. Results are representative of at least 3 experiments. (**C and D**) Costaining of CALB (green) and MBP (red) in DCN of *Nes-Wdr45*$^{fl/+}$ and *Nes-Wdr45*$^{fl/fl}$ female mice at 13 mo. Quantification data are shown as mean ±SEM of 3 mice (1 unit = 10^4 μm^2) (**D**). (**E and F**) SQSTM1 (red) and Ubiquitin (green) costaining in DCN of *Nes-Wdr45*$^{fl/+}$ and *Nes-Wdr45*$^{fl/fl}$ female mice at 13 mo. Quantification data are shown as mean ± SEM of 3 mice (1 unit = 10^4 μm^2) (**F**). Bar: 10 μm (**C and E**).

already become evident. Moreover, iron accumulation is sometimes absent even in patients with demonstrable mutations in the causative genes associated with NBIA.[12]

Mice deficient for autophagy genes that function at distinct steps show distinct neuropathological deficits. Neural-specific depletion of *Atg5, Atg7*, and *Ei24* causes massive neuron loss, while *Epg5*-deficient mice exhibit selective vulnerability of motor neurons.[5-7,16] *Epg5* acts at a late step of autophagy and loss of function of *Epg5* causes accumulation of nondegradative autolysosomes.[16] *epg-6* acts at an early step of autophagosome formation.[3] However, compared to *Atg5-, Atg7-*, and *Ei24*-deficient mice, both the autophagy defect and the neural damage are much milder in *Nes-Wdr45*$^{fl/Y}$ mice, which could be because the other 3 *Wipi*-family genes, *Wipi1, Wipi2*, and *Wdr45b*/*Wipi3*, function redundantly in the autophagy pathway.[19] Axon spheroids represent swollen or distended axons, possibly secondary to defects in axonal transport. Autophagy is required for normal axon terminal membrane trafficking and turnover, and plays an essential role in the maintenance of axonal homeostasis and prevention of axonal degeneration.[20,21] Accumulation of axonal spheroid structures in *Wdr45* mice indicates that axoN-terminals are more vulnerable to autophagy impairment than dendrites and neurons. Purkinje cell-specific deletion of *Atg7* shows that ablation of autophagy leads to abnormal swellings and dystrophy of axon terminals in the DCN, preceding the dentritic atrophy, neuron loss, and behavioral deficits.[22] Another possibility is that

Wdr45 may have some functions independent of autophagy, which are important for maintaining neural homeostasis and learning and memory ability. Autophagy proteins also function in autophagy-independent processes.[23] For example, the essential autophagy gene *Atg5* is required for cellular immunity to intracellular pathogens via autophagosome-independent processes such as GTPase trafficking.[24] The *Nes-Wdr45*$^{fl/Y}$ mice provide a valuable model for understanding the neurodegeneration process underlying the pathogenesis of BPAN, and also for preclinical testing and exploration of therapeutic interventions.

Materials and Methods

Mice

The *Wdr45* targeting vector was constructed by flanking exons 8 to 14 of *Wdr45* by 2 *loxP* sequences. After electroporating the linearized vector into 129 R1 embryonic stem cells, positive clones with homologous recombinants were identified by Southern blot analysis, as shown in **Figure 1B**. Southern blot analysis was performed by digestion of genomic DNA with SpeI and hybridization with the 5′ probe (or NdeI and hybridization with 3′ probe). The positive clone was then microinjected into C57BL/6N blastocysts. Chimeric males were mated with wild-type C57BL/6N females, and heterozygous and hemizygous mutant offspring were backcrossed to C57BL/6 mice.

All mice were kept under specific pathogen-free conditions in the animal facility at the Institute of Biophysics, Chinese Academy of Sciences, Beijing. All animal experiments were approved by the institutional committee of the institute.

Antibodies

The following antibodies were used: rabbit anti-SQSTM1 (MBL, PM045), mouse anti-SQSTM1 (Abcam, ab56416), mouse anti-ubiquitin (Cell Signaling Technology, 3936), rabbit anti-GFAP (Bioss, bs-0199R), mouse anti-RBFOX3/NeuN (Millipore, MAB377), rabbit anti-LC3 (Cell Signaling Technology, 2775S), mouse anti-CALB/calbindin (Sigma, C9848), rabbit anti-CALB/calbindin (Abcam, ab25085), rabbit anti-ATG9 (MBL, PD042), and rabbit anti-MBP (Abcam, ab40390).

Rotarod test

Motor coordination was measured as described previously with some modifications.[7] After trained on the rolling rod at 5 rpm for 5 min for one d, mice were tested for their ability to remain on the rotarod at 5, 10, 20, and 40 rpm. The time when the mice fell from the rod was recorded, with a maximum observation time of 5 min.

Morris water maze test

A round tub (diameter 120 cm, height 45 cm) was filled with opaque water (20°C) to a depth of 25 cm. A platform (diameter 9 cm, height 24 cm) was located in the center of one quadrant. In the learning test, the mouse was placed in the maze starting from one of 4 predetermined spots and was given 60 s to find the fixed platform. The time taken to reach the platform (escaping latency) was recorded by a Smart 2.0 video tracking system (Panlab, Harvard Apparatus, Cornellà (Barcelona), Spain). Each mouse received 4 trials per day for 6 consecutive d. On the 7th d, the probe test was performed without the platform. The mouse was allowed to search for 60 s, and the percentage of time spent in the target quadrant was recorded to monitor spatial memory ability.

Y-maze test

Mice were individually placed into the center of a symmetrical Y-maze with 3 arms, and allowed to freely enter the arms during an 8-min session. The series of arm entries was recorded visually. The percentage of alternation was calculated as the ratio of correct alternations (successive entry into the 3 arms on overlapping triplet sets) to total alternations.

Fear conditioning test

The fear conditioning test was performed using the Startle and Fear combined system (Panlab, Harvard Apparatus, Cornellà (Barcelona), Spain). For training, after 10-min acclimation, mice were placed in a chamber, and a 70 dB tone was delivered for 30 s as a conditioned stimulus. During the last 2 s, a foot shock of 0.4 mA was delivered through a shock generator. This procedure was repeated 6 times at 15-s intervals. Animal movement was recorded through a high-sensitivity weight transducer system by PACKWIN software. On the second d, for the contextual test, mice were placed in the chamber, and the freezing response was measured for 2 min without the conditioned stimulus. For the cued test, the freezing response was measured with the conditioned stimulus.

Electrophysiology

Mice were sacrificed, and transverse hippocampal slices (400 μm) were prepared using a vibratome (VT1200S, Leica, Wetzlar, Germany) in oxygenated (95% O_2 and 5% CO_2) ice-cold artificial cerebrospinal fluid (ACSF, 126 mM NaCl, 3 mM KCl, 26 mM $NaHCO_3$, 1.2 mM NaH_2PO_4, 10 mM D-glucose, 2.4 mM $CaCl_2$ and 1.3 mM $MgCl_2$). The slices were kept in an incubating chamber filled with oxygenated ACSF at 28 to 30°C. After a recovery period of at least 60 min, an individual slice was transferred to a recording chamber and was continuously superfused with oxygenated ACSF (5 ml/min) at 30°C.

fEPSPs were recorded using ACSF-filled glass pipettes (1 to 3 MΩ) placed at the stratum radiatum of area CA1. fEPSPs were evoked using a concentric bipolar electrode (WPI; FHC, CBBEB75) which was used to stimulate the SC fibers with a brief current pulse (50 μs), and the current pulse was delivered by a stimulus isolation unit (ISO-Flex,A.M.P.I., Jerusalem, Israel) every 30s. The distance between stimulating electrode and recording pipette was 200 to 300 μm. An input-output curve was used to set the stimulating strength, which yielded 30 to 50% of the maximal slope. After obtaining baseline measurements for 20 min, LTP was induced using θ-burst stimulation (each burst contained 5 pulses at 100 Hz repeated at 5 Hz and 3 10-burst trains separated by 20 s). Evoked fEPSPs were recorded for 1 h after tetanization. Signals were filtered at 2 kHz and

digitized at 100 kHz using Digidata 1440A (Molecular Devices). Data acquisition and slope measurement were carried out using pClamp 10.2 (Molecular Devices). Pulse generation was achieved using a Master 8 stimulator (A.M.P.I., Jerusalem, Israel).

Primary neuron culture Primary cortical neurons were harvested from embryonic d 18 pups. Cerebral cortices were collected and dissociated by incubation in TypLE^{EM} express enzymes (Gibco, 12605010) for 30 min at 37°C. After termination with FBS, cells were centrifuged at 217 g for 2 min, and plated with Neurobasal medium (Invitrogen, 10888022) supplemented with B27 (Invitrogen, 17504044), penicillin/streptomycin, Glutamax (Invitrogen, 35050061) and 5% FBS (HyClone Laboratories, SH3008403) on 35-mm dishes (BD Falcon, 353001) precoated with poly-d-lysine (100 μg/ml, Sigma, P1524). After incubation at 37°C for at least 4 h, the plating medium was changed to Neurobasal medium containing B27, penicillin/streptomycin, and Glutamax. Half the volume of culture medium was changed every 3 d For lysosome function inhibition, cells were treated with 20 μM bafilomycin A_1 (Sigma, B1793) for 6 h before harvest.

Histology and immunofluorescence staining

After transcardial perfusion with 10% neutral buffered formalin (Sigma, HT501128), CNS tissues were post-fixed, dehydrated, embedded in paraffin, and sectioned at 5 μm. Sections were stained with hematoxylin and eosin for histological examination and signals were acquired by light microscopy (Imager A1, Zeiss, Göttingen, Germany) with a 40×/0.75 objective lens (Plan-NeoFluar, Zeiss, Göttingen, Germany) and a camera (AxioCam MRc5, Zeiss, Göttingen, Germany) at RT. Images were processed and viewed using AxioVision 40v4.6.3.0 software.

For immunostaining, after deparaffinization and rehydration, heat-induced epitope retrieval (0.1 M citrate buffer) was performed on sections. Samples were then blocked with normal goat serum and incubated with primary antibodies at 4°C overnight in a humidity chamber. After incubation, sections were washed in phosphate-buffered saline (137 mM NaCl, 2.7 mM KCl, 10 mM Na_2HPO_4, 2.0 mM KH_2PO_4, pH 7.2) 3 times, and incubated with fluorescently-labeled secondary antibodies (Jackson ImmunoResearch Laboratories, 111–095–003, 111–025–003, 115–025–003, 115–095–003) for 1 h at room temperature. Finally, sections were counterstained with DAPI, mounted and examined under a confocal microscope (Zeiss LSM 710 Meta plus Zeiss Axiovert zoom, Göttingen, Germany) with a 63×/1.40 oil-immersion objective lens (Plan-Apochromatlan, Zeiss, Göttingen, Germany) and a camera (AxiocamHRm, Zeiss, Göttingen, Germany) at RT. Images were processed and viewed using ZEN 2011 software.

Immunoblotting

Cells were lysed with RIPA buffer (50 mM Tris-HCl, pH 7.4, 150 mM NaCl, 1 mM EDTA, 0.1% SDS [SERVA, 20765.03], 1% NP40 [Amresco, E109]) supplemented with protease inhibitor cocktail (Roche, 04693116001), and incubated on ice for 30 min. Homogenates were centrifuged at 13,000 rpm for 10 min at 4°C. Supernatant fractions were collected and protein concentrations were determined by Bradford protein assay (Genstar, E161–01). Equal amounts (20 to 30 μg) of proteins were subjected to SDS-PAGE electrophoresis, transferred to a PVDF membrane and then blocked with 5% nonfat milk for 1 h at room temperature, membranes were incubated with primary antibodies at 4°C overnight. After washing with PBST (0.5% Tween 20 [Amresco, 0777] in PBS) 3 times, the membranes were incubated with HRP-labeled secondary antibodies (Sigma, A0545, A9044) for 1 h at room temperature. Immunoreactivity was determined using an Enhanced Chemiluminescent kit (GE, RPN2232).

Proteasome activity assay

Mice cerebral tissues were homogenized in lysis buffer (50 mM HEPES, pH 7.5, 5 mM EDTA, 150 mMNaCl, 1% Triton X-100 [Amresco, 0694] and 2 mM ATP). 250 μl lysate containing equal amounts of protein (2 to 4 μg) were incubated for 30 min at 37°C in the dark with 2.5 μl of each substrate (final concentration: 50 nM). Aminomethylcoumarin (AMC)-linked synthetic peptide substrates, Ac-Gly-Pro-Leu-Asp-AMC, Suc-Leu-Leu-Val-Tyr-AMC or Ac-Arg-Leu-Arg-AMC (and Boc-Leu-Arg-Arg-AMC), were used for detecting caspase-like, chymotrypsin-like, or trypsin-like activity, respectively (Proteasome Substrate Pack, Enzo Life Sciences, PW9905–0001). The reaction was stopped by adding 252.5 μl precooled 96% ethanol solution. Proteasome activity was measured by detecting fluorescence from AMC hydrolysis (380 nm excitation and 460 nm emission).

Transmission electron microscopy

Mice were transcardially perfused, and cerebral tissues were dissected and postfixed in 2.5% glutaraldehyde. Then samples were fixed with 1% OsO_4 for 2 h, followed by dehydration with graded ethanol solutions, and embedded in Embed812 (Electron Microscopy Sciences, 14120). Ultrathin sections were cut at 80 nm, stained with 2% uranyl acetate for 30 min and lead citrate for 10 min. The samples were examined using a 120 kV electron microscope (FEI, Tecnai Spirit, Oregon, USA) at 80 kV and images were captured with a CCD camera (FEI, Eagle, Oregon, USA) using Digital Micrograph software at RT.

Quantitative RT-PCR

Total RNA was extracted using TRIzol (Invitrogen, 15596018) and cDNA was synthesized by Super Script® III First-Strand Kit (Invitrogen, 11752050). Quantitative PCR was performed on a StepOnePlus™ Real-Time PCR system (Applied Biosystems, CA, USA) using SYBR® Premix Ex Taq™ (TaKaRa, RR820A).

The following primers were used:

F-*Wdr45*: 5′-CATCTTGACCACGAGCAGGT-3′
R-*Wdr45*: 5′-GAAGGTGAACTCCAGCACCA-3′
F-*Sqstm1*: 5′-GCTGCCCTATACCCACATCT-3′
R-*Sqstm1*: 5′-CGCCTTCATCCGAGAAAC-3′
F-*Actb* (β-actin): 5′-CTGGCTCCTAGCACCATGAAGAT-3′
R-*Actb*: 5′-GGTGGACAGTGAGGCCAGGAT-3′

Statistical analysis

Statistical significance was calculated by the Student *t* test. A *P* value less than 0.05 was considered significant.

Disclosure of Potential Conflicts of Interest

No potential conflicts of interest were disclosed.

Acknowledgments

We are grateful to the National Institute of Biological Sciences Transgenic Research Center for generating *Wdr45* conditional KO mice, and Dr. Isabel Hanson for editing work. We also thank the animal facility at the Institute of Biophysics, Chinese Academy of Sciences for mice maintenance. Electron microscopy work was performed at the Center for Biological Imaging (http://cbi.ibp.ac.cn), Institute of Biophysics.

Funding

This work was supported by the National Natural Science Foundation of China (31421002, 31225018), grants from the National Basic Research Program of China (2013CB910100, 2011CB910100) to HZ, and also a grant from the National Natural Science Foundation of China (31401184) to YGZ. The research of Hong Zhang was supported in part by an International Early Career Scientist grant from the Howard Hughes Medical Institute.

References

1. Nakatogawa H, Suzuki K, Kamada Y, Ohsumi Y. Dynamics and diversity in autophagy mechanisms: lessons from yeast. Nat Rev Mol Cell Biol 2009; 10:458-67; PMID:19491929; http://dx.doi.org/10.1038/nrm2708.
2. Tian Y, Li Z, Hu W, Ren H, Tian E, Zhao Y, Lu Q, Huang X, Yang P, Li X, et al. *C. elegans* screen identifies autophagy genes specific to multicellular organisms. Cell 2010; 141:1042-55; PMID:20550938; http://dx.doi.org/10.1016/j.cell.2010.04.034.
3. Lu Q, Yang P, Huang X, Hu W, Guo B, Wu F, Lin L, Kovács AL, Yu L, Zhang H. The WD40 repeat PtdIns (3)P-binding protein EPG-6 regulates progression of omegasomes to autophagosomes. Dev Cell 2011; 21:343-57; PMID:21802374; http://dx.doi.org/10.1016/j.devcel.2011.06.024.
4. Levine B, Kroemer G. Autophagy in the pathogenesis of disease. Cell 2008; 132:27-42; PMID:18191218; http://dx.doi.org/10.1016/j.cell.2007.12.018.
5. Hara T, Nakamura K, Matsui M, Yamamoto A, Nakahara Y, Suzuki-Migishima R, Yokoyama M, Mishima K, Saito I, Okano H, et al. Suppression of basal autophagy in neural cells causes neurodegenerative disease in mice. Nature 2006; 441:885-9; PMID:16625204; http://dx.doi.org/10.1038/nature04724.
6. Komatsu M, Waguri S, Chiba T, Murata S, Iwata J, Tanida I, Ueno T, Koike M, Uchiyama Y, Kominami E, et al. Loss of autophagy in the central nervous system causes neurodegeneration in mice. Nature 2006; 441:880-4; PMID:16625205; http://dx.doi.org/10.1038/nature04723.
7. Zhao YG, Zhao H, Miao L, Wang L, Sun F, Zhang H. The p53-induced gene Ei24 is an essential component of the basal autophagy pathway. J Biol Chem 2012; 287:42053-42063; PMID:23074225; http://dx.doi.org/10.1074/jbc.M112.415968.
8. Haack TB, Hogarth P, Kruer MC, Gregory A, Wieland T, Schwarzmayr T, Graf E, Sanford L, Meyer E, Kara E, et al. Exome sequencing reveals de novo WDR45 mutations causing a phenotypically distinct, X-linked dominant form of NBIA. Am J Hum Genet 2012; 91:1144-9; PMID:23176820; http://dx.doi.org/10.1016/j.ajhg.2012.10.019.
9. Hayflick SJ, Kruer MC, Gregory A, Haack TB, Kurian MA, Houlden HH, Anderson J, Boddaert N, Sanford L, Harik SI, et al. β-Propeller protein-associated neurodegeneration: a new X-linked dominant disorder with brain iron accumulation. Brain 2013; 136:1708-17; PMID:23687123; http://dx.doi.org/10.1093/brain/awt095.
10. Saitsu H, Nishimura T, Muramatsu K, Kodera H, Kumada S, Sugai K, Kasai-Yoshida E, Sawaura N, Nishida H, Hoshino A, et al. De novo mutations in the autophagy gene WDR45 cause static encephalopathy of childhood with neurodegeneration in adulthood. Nat Genet 2013; 45:445-9; PMID:23435086; http://dx.doi.org/10.1038/ng.2562.
11. Gregory A, Polster BJ, Hayflick SJ. Clinical and genetic delineation of neurodegeneration with brain iron accumulation. J Med Genet 2009; 46:73-80; PMID:18981035; http://dx.doi.org/10.1136/jmg.2008.061929.
12. Schneider SA, Bhatia KP. Syndromes of neurodegeneration with brain iron accumulation. Semin Pediat Neurol 2012; 19:57-66; http://dx.doi.org/10.1016/j.spen.2012.03.005.
13. D'Hooge R, De Deyn PP. Applications of the Morris water maze in the study of learning and memory. Brain Research Reviews. Brain Res Rev 2001; 36:60-90; PMID:11516773; http://dx.doi.org/10.1016/S0165-0173(01)00067-4.
14. Packard MG, Cahill L. Affective modulation of multiple memory systems. Curr Opin Neurobiol 2001; 11:752-6; PMID:11741029; http://dx.doi.org/10.1016/S0959-4388(01)00280-X.
15. Malenka RC. The long-term potential of LTP. Nat Rev Neurosci 2003; 4:923-6; PMID:14595403; http://dx.doi.org/10.1038/nrn1258.
16. Zhao H, Zhao YG, Wang X, Xu L, Miao L, Feng D, Chen Q, Kovács AL, Fan D, Zhang H. Mice deficient in *Epg5* exhibit selective neuronal vulnerability to degeneration. J Cell Biol 2013; 200:731-41; PMID:23479740; http://dx.doi.org/10.1083/jcb.201211014.
17. Mizushima N, Yoshimori T, Levine B. Methods in mammalian autophagy research. Cell 2010; 140:313-26; PMID:20144757; http://dx.doi.org/10.1016/j.cell.2010.01.028.
18. Phillips RG, LeDoux JE. Differential contribution of amygdala and hippocampus to cued and contextual fear conditioning. Behav Neurosci 1992;106:274-85; PMID:1590953; http://dx.doi.org/10.1037/0735-7044.106.2.274.
19. Dooley HC, Razi M, Polson HE, Girardin SE, Wilson MI, Tooze SA.WIPI2 links LC3 conjugation with PI3P, autophagosome formation, and pathogen clearance by recruiting Atg12-5-16L1. Mol Cell 2014; 55:238-52; PMID:24954904; http://dx.doi.org/10.1016/j.molcel.2014.05.021.
20. Lee S, Sato Y, Nixon RA. Lysosomal proteolysis inhibition selectively disrupts axonal transport of degradative organelles and causes an Alzheimer-like axonal dystrophy. J Neurosci 2011; 31:7817-30; PMID:21613495; http://dx.doi.org/10.1523/JNEUROSCI.6412-10.2011.
21. Maday S, Wallace KE, Holzbaur EL. Autophagosomes initiate distally and mature during transport toward the cell soma in primary neurons. J Cell Biol 2012; 196:407-17; PMID:22331844; http://dx.doi.org/10.1083/jcb.201106120.
22. Komatsu M, Wang QJ, Holstein GR, Friedrich VL Jr, Iwata J, Kominami E, Chait BT, Tanaka K, Yue Z. Essential role for autophagy protein Atg7 in the maintenance of axonal homeostasis and the prevention of axonal degeneration. Proc Natl Acad Sci USA 2007; 104:14489-94; PMID:17726112; http://dx.doi.org/10.1073/pnas.0701311104.
23. Subramani S, Malhotra V. Non-autophagic roles of autophagy-related proteins. EMBO Rep 2013; 14(2):143-51; PMID:23337627; http://dx.doi.org/10.1038/embor.2012.220.
24. Zhao Z, Fux B, Goodwin M, Dunay IR, Strong D, Miller BC, Cadwell K, Delgado MA, Ponpuak M, Green KG, et al. Autophagosome-independent essential function for the autophagy protein Atg5 in cellular immunity to intracellular pathogens. Cell Host Microbe 2008;4:458-69; PMID:18996346; http://dx.doi.org/10.1016/j.chom.2008.10.003.